Viscous Compressible Flow in the Boundary Region of an Axial Corner

A. G. Mikhail* and K. N. Ghia†
University of Cincinnati, Cincinnati, Ohio

Laminar flow along a 90-deg corner, formed by the intersection of two semi-infinite flat plates, is analyzed, under the assumption of shock-free supersonic flow. The analysis is based on the method of matched asymptotic expansions. Numerical solutions are obtained for the streamwise self-similar corner flow, using the ADI method. Appropriate mapping functions are employed, so that the far-field boundary conditions are imposed at true infinity. Results are presented for subsonic and supersonic flows, with adiabatic as well as heat-transfer wall conditions. The effects of location of the far-field boundary and of the model-fluid assumption are assessed accurately. Effects of Prandtl number, viscosity law, and level of freestream temperature on the solutions are also studied. The numerical method developed is efficient and the optimization techniques implemented have wider applications. A numerical "compressibility-transformation" is also suggested for obtaining a suitable finite-difference grid for highly supersonic flows.

I. Introduction

THE high-speed flow past a general aerodynamic configuration encounters strong viscous-inviscid interactions, which have been shown to influence the flowfield significantly. One such configuration of great interest is the axial corner formed by intersecting compression surfaces. The interactions evolve due to the very nature of compression surfaces, which are inclined at some angle to the freestream, and also as a result of boundary-layer displacement effects. Consequently, the resulting flowfield contains regions involving vortices and complicated shock structure characterized by embedded shocks. Further, the interaction of the shock waves with the boundary layers causes flow separation as well as localized high-heating regions[1] which can lead to component failure. Because of the importance of these interactions, which have the potential to alter the flowfield drastically and, thereby, degrade the overall aerodynamic performance, it is essential to investigate fully the characteristic features of the axial corner flow. There are a few basic corner configurations which are generally found in components of a high-speed vehicle, namely, wing-body and wing-fin junctions, engine inlets, and at the intersections of blades with the hub and the shroud in turbomachines.

In a comprehensive survey article, Korkegi[1] has reviewed the high-speed viscous interaction phenomena, and has thoroughly documented the available investigations on axial-corner flow. He has also reported the excellent work of Charwat and Redekeopp,[2] who were the first to construct, in accord with their experiments, the detailed shock structure for supersonic flow along an axial corner formed by the intersection of two wedges. These shock waves impinge on the viscous boundary region of the corner and lead to a complex flowfield that is very difficult to model analytically. Using a shock-capturing technique, Kutler[3] has successfully simulated the inviscid shock structure numerically for this corner geometry. On the other hand, in another important review article, Bloom et al.[4] suggested that, for the very basic configuration of a 90-deg axial corner formed by intersection of two plates, shock-wave boundary-layer interactions are negligible for supersonic flow, and the effect of compressibility can be included in a straightforward manner with the assumption of shock-free flow. These findings[4] permit a valid shock-free analysis of the viscous region of the flat-plate axial corner problem.

Rubin[5] provided a firm analytical foundation to study the viscous boundary region of axial corner flow. A majority of the theoretical efforts pursued thereafter have used Rubin's basic analysis of incompressible corner flow. After an early investigation of the incompressible problem,[6] the effect of compressibility was introduced in the corner flow problem by Weinberg and Rubin,[7] and results were obtained for Mach number M_∞ ranging from 0.0 to 2.0 and for various thermal conditions at the wall boundary. Their analysis was valid in the absence of viscous-inviscid interactions, for shock-free flow of a model fluid, i.e., for Prandtl number Pr equal to unity and linear viscosity law.

The compressible corner flow was also analyzed by Ghia and Davis,[8] who provided efficient numerical solutions for the corresponding incompressible problem. For the general compressible fluid, the asymptotic viscous flow, to lowest order, for the corner problem has also been calculated by Ghia and Davis.[9] This asymptotic analysis[9] recovers all available lowest-order asymptotic solutions of Libby,[10] Bloom,[11] and Weinberg and Rubin[7] for a model fluid. The need for determining the higher-order asymptotic solutions[6,7] for posing the far-field boundary condition at a finite distance can be circumvented by analyzing the infinite or unbounded corner region as done by Ghia[12] for the incompressible case.

The objectives of the present study are threefold. First, it is desired to introduce the effect of compressibility in the earlier analysis of Ghia[12] and develop an efficient and reliable scheme for the determination of unbounded compressible corner flow. The second objective is to assess the effect of the location of the far-field boundary and the assumption of a model fluid on the solutions. Finally, it is desired to perform a parametric study for the problem over a wide range of values of the important flow parameters and, thus, provide the first set of results for unbounded corner flow for a general compressible fluid.

Presented as Paper 77-685 at the AIAA 10th Fluid and Plasmadynamics Conference, Albuquerque, N. Mex., June 27-29, 1977; submitted July 25, 1977; revision received April 28, 1978.

Index categories: Viscous Nonboundary-Layer Flows; Computational Methods.

*Research Associate, Dept. of Aerospace Engineering and Applied Mechanics. Present Address: Air Force Flight Dynamics Laboratory, Wright-Patterson Air Force Base, Ohio. Member AIAA.

†Associate Professor, Dept. of Aerospace Engineering and Applied Mechanics. Member AIAA.

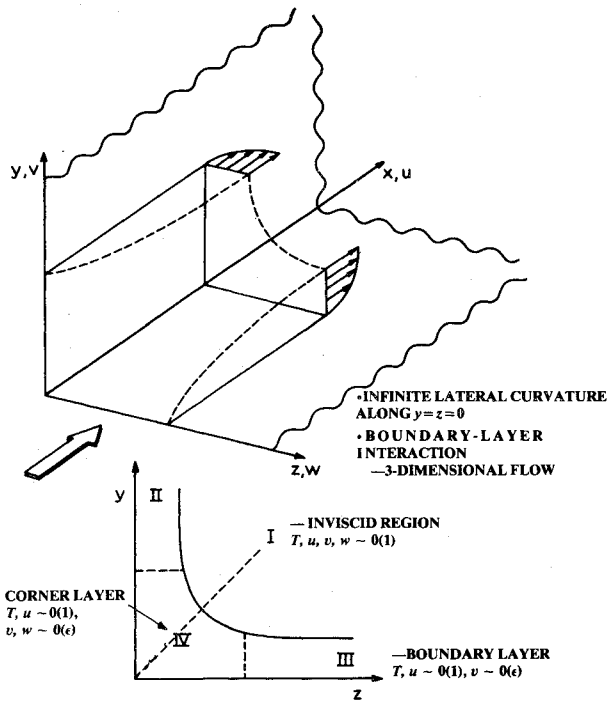

Fig. 1 Corner flow configuration.

II. Mathematical Model

The analysis needed for formulating the mathematical model is very similar to that used by Ghia[12] for the corresponding unbounded incompressible problem. Hence, only brief comments about it will be made here, with the governing differential equations being presented directly, without describing the details of their derivation. The analysis is based on the method of singular perturbations and matched asymptotic expansions. Only the viscous interactions between the boundary layers on the two intersecting walls are included in the analysis and, further, it is assumed that the supersonic flowfield is free of shock waves. Figure 1 delineates the axial corner geometry where the three-dimensional "corner layer" is represented as region IV; also shown in this figure are the boundary-layer regions II and III as well as the inviscid region I.

In the absence of a streamwise pressure gradient, the flow exhibits similarity along the x direction far downstream from the leading edge. The use of similarity coordinates (η,ζ) and appropriate similarity form of dependent variables gives rise to a set of corner-layer equations[13] in the similarity plane (η,ζ). These nonlinear coupled partial differential equations are elliptic in nature, so that boundary conditions are required on the entire boundary of a closed domain. Invoking the symmetry of the flow across the corner bisector (see Fig. 1), only one triangular region needs to be considered for the solution. Therefore, boundary conditions are required on the boundary of the domain comprised by the $\eta=0$ surface, the corner bisector line $\eta=\zeta$, and the far-field boundary at $\zeta\to\infty$ for all η. To facilitate the placement of this far-field boundary at true infinity and, thereby, avoid the tedious algebra of the higher-order asymptotic analysis, the infinite corner region, in stretched similarity variables, is transformed to a finite region in terms of new coordinates (N,S) where $N=\eta/(c+\eta)$ and $S=\zeta/(c+\zeta)$, so that $0\le N,\ S\le 1$; here, c is a constant.[12] The form of the transformation is based on the asymptotic behavior of the flow; this prevents the development of any anamolies or singularities in the flow variables with respect to the transformed coordinates. The transformation also allows for suitably stretching regions of flow where steep gradients may exist, leading thereby to improved accuracy in the ensuing finite-difference calculations. Some of the dependent variables used in the finite-corner formulation become unbounded as η or $\zeta\to\infty$. Therefore, new dependent variables, denoted here with an overbar, are also defined such that these new variables remain finite everywhere in the infinite region of the corner. The final form of the lowest-order corner-layer equations, in nondimensional form, are given as follows:

Energy Equation

$$\frac{\bar\mu}{Pr}N_\eta^2\bar T_{NN}+\frac{\bar\mu}{Pr}S_\zeta^2\bar T_{SS}+\left[\frac{\bar\mu}{Pr}N_{\eta\eta}+N_\eta\left(\frac{1}{Pr}\bar\mu_N N_\eta+\bar\rho\phi\right)\right]\bar T_N$$
$$+\left[\frac{\bar\mu}{Pr}S_{\zeta\zeta}+S_\zeta\left(\frac{1}{Pr}\bar\mu_S S_\zeta+\bar\rho\psi\right)\right]\bar T_S+(\gamma-1)M_\infty^2\bar\mu$$
$$\times[\bar u_N^2N_\eta^2+\bar u_S^2S_\zeta^2]=0 \tag{1}$$

Streamwise Momentum Equation

$$\bar\mu N_\eta^2\bar u_{NN}+\bar\mu S_\zeta^2\bar u_{SS}+[\bar\mu N_{\eta\eta}+N_\eta(\bar\rho\phi+\bar\mu_N N_\eta)]\bar u_N+[\bar\mu S_{\zeta\zeta}$$
$$+S_\zeta(\bar\rho\psi+\bar\mu_S S_\zeta)]\bar u_S=0 \tag{2}$$

Continuity Equation

$$\bar\Lambda=2\bar u-(1/\bar\rho)[\phi\bar\rho_N N_\eta+\psi\bar\rho_S S_\zeta]-(u_2+u_1) \tag{3}$$

Equation for $\bar\phi$

$$N_\eta^2\bar\phi_{NN}+S_\zeta^2\bar\phi_{SS}+N_{\eta\eta}\bar\phi_N+S_{\zeta\zeta}\bar\phi_S+(\bar\theta_S S_\zeta-\bar\Lambda_N N_\eta)=0 \tag{4}$$

Equation for $\bar\psi$

$$N_\eta^2\bar\psi_{NN}+S_\zeta^2\bar\psi_{SS}+N_{\eta\eta}\bar\psi_N+S_{\zeta\zeta}\bar\psi_S-(\bar\theta_N N_\eta+\bar\Lambda_S S_\zeta)=0 \tag{5}$$

Modified Streamwise Vorticity Equation

$$\bar\mu N_\eta^2\bar\theta_{NN}+[\bar\mu N_{\eta\eta}+N_\eta(\bar\rho\phi+2\bar\mu_N N_\eta)]\bar\theta_N+\bar\mu S_\zeta^2\bar\theta_{SS}$$
$$+[\bar\mu S_{\zeta\zeta}+S_\zeta(\bar\rho\psi+2\bar\mu_S S_\zeta)]\bar\theta_S+2\bar\rho\bar u\bar\theta+(\zeta u_2''-u_1')$$
$$\cdot(\bar\rho\phi+2\bar\mu_N N_\eta)+(u_2'-\eta u_1'')(\bar\rho\psi+2\bar\mu_S S_\zeta)+2\bar\rho\bar u(\zeta u_2'-\eta u_1')$$
$$+\bar\mu(\zeta u_2'''-\eta u_1''')+(\bar\mu_{NN}N_\eta^2+\bar\mu_N N_{\eta\eta}-\bar\mu_{SS}S_\zeta^2-\bar\mu_S S_{\zeta\zeta})$$
$$\cdot(\phi S_\zeta+\psi_N N_\eta)+\eta(\bar u^2\bar\rho_S S_\zeta+2\bar\rho\bar u\bar u_S S_\zeta)$$
$$-\zeta(\bar u^2\bar\rho_N N_\eta+2\bar\rho\bar u\bar u_N N_\eta)-\phi(\bar\rho_S S_\zeta\phi_N N_\eta-\bar\rho_N N_\eta\phi_S S_\zeta)$$
$$-\psi(\bar\rho_S S_\zeta\psi_N N_\eta-\bar\rho_N N_\eta\psi_S S_\zeta)+2N_\eta S_\zeta[\bar\mu_N(\Lambda_S-\bar u_S)$$
$$-\bar\mu_S(\Lambda_N-\bar u_N)+\bar\mu_{NS}(\psi_S S_\zeta-\phi_N N_\eta)]=0 \tag{6}$$

The auxiliary equations required to close this set of equations are:

Equation of State

$$\bar p=\bar\rho\bar T(1/\gamma M_\infty^2) \tag{7}$$

Sutherland's Viscosity Law

$$\bar\mu=\bar T^{3/2}[(1+S_1)/(\bar T+S_1)] \tag{8}$$

where γ is the ratio of specific heats and S_1 is a parameter that depends on the freestream temperature T_∞.

The similarity form of the dependent variables $\bar u$, $\bar\phi$, $\bar\psi$, $\bar\theta$ is defined in Eq. (11) of Ref. 12; the remaining variables $\bar T$, $\bar\rho$, $\bar\mu$, and $\bar\Lambda$ are defined as follows:

$$\bar T(\eta,\zeta)=T(\eta,\zeta),\bar\rho(\eta,\zeta)=\rho(\eta,\zeta),\bar\mu(\eta,\zeta)=\mu(\eta,\zeta),$$
$$\bar\Lambda(\eta,\zeta)=\Lambda(\eta,\zeta)-u(\infty,\zeta)-u(\eta,\infty) \tag{9}$$

Also, for convenience of writing, ϕ, ψ, and Λ have been retained in unbarred form in Eqs. (1-3, and 6). In the numerical calculations, these are replaced appropriately by their definitions in terms of the barred variables as $\phi(\eta,\zeta)=\bar{\phi}(\eta,\zeta)+\eta u(\infty,\zeta)$ and $\psi(\eta,\zeta)=\bar{\psi}(\eta,\zeta)+\zeta u(\eta,\infty)$. In addition, $u_1 \triangleq u(\infty,\zeta)$, $u_2 \triangleq u(\eta,\infty)$, and primes denote differentiation with respect to coordinates. The boundary conditions for Eqs. (1-6) in the computational domain are given as follows:

1) At the wall $N=0$:

$$\bar{T}(0,S)=\bar{T}_w \text{ or } \bar{T}_N(0,S)=0 \tag{10a}$$

$$\bar{u}(0,S)=0,\ \bar{\phi}(0,S)=0,\ \bar{\psi}(0,S)=0 \tag{10b}$$

$$\bar{\theta}(0,S)=\bar{\psi}_N(0,S)N_\eta(0),\ \bar{\Lambda}(0,S)=-u(1,S) \tag{10c}$$

2) At the line of symmetry $N=S$: At this boundary, $\bar{T}$, $\bar{u},\bar{\phi},\bar{\psi}$, and $\bar{\Lambda}$ are obtained by solving their respective governing equations at the line of symmetry, implicitly using the conditions

$$\bar{F}(N,S)=\bar{F}(S,N) \tag{11a}$$

where $\bar{F}$ denotes $\bar{T},\bar{u},\bar{\Lambda},\bar{\mu}$, or $\bar{\rho}$,

$$\bar{\phi}(N,N)=\bar{\psi}(N,N),\ \bar{\theta}(N,N)=0 \tag{11b}$$

3) At the far-field boundary $S=1$, for all N: The lowest-order corner-layer equations (1-6) automatically reduce to their correct limiting form for yielding the proper asymptotic boundary conditions for the problem. These equations are

$$\frac{\bar{\mu}}{Pr}N_\eta^2\bar{T}_{NN}+\left[\frac{\bar{\mu}}{Pr}N_{\eta\eta}+N_\eta\left(\frac{1}{Pr}\bar{\mu}_N N_\eta+\bar{\rho}(\bar{\phi}+\eta)\right)\right]T_N$$
$$+(\gamma-1)M_\infty^2\bar{\mu}\bar{u}_N^2N_\eta^2=0 \tag{12}$$

$$\bar{\mu}N_\eta^2\bar{u}_{NN}+[\bar{\mu}N_{\eta\eta}+N_\eta(\bar{\rho}(\bar{\phi}+\eta))+\bar{\mu}_N N_\eta]\bar{u}_N=0 \tag{13}$$

$$\bar{\Lambda}=\bar{u}\frac{1}{\bar{\rho}}(\bar{\phi}+\eta)\bar{\rho}_N N_\eta-1 \tag{14}$$

$$N_\eta^2\bar{\phi}_{NN}+N_{\eta\eta}\bar{\phi}_N-\bar{\Lambda}_N N_\eta=0 \tag{15}$$

$$N_\eta^2\bar{\psi}_{NN}+N_{\eta\eta}\bar{\psi}_N-\bar{\theta}_N N_\eta=0 \tag{16}$$

$$\bar{\mu}N_\eta^2\bar{\theta}_{NN}+[\bar{\mu}N_{\eta\eta}+N_\eta(\bar{\rho}(\bar{\phi}+\eta)+2\bar{\mu}_N N_\eta)]\bar{\theta}_N$$
$$+[2\bar{\rho}\bar{u}+\bar{\mu}_{NN}N_\eta^2+\bar{\mu}_N N_{\eta\eta}]\bar{\theta}+\bar{u}\bar{\psi}\bar{\rho}_N N_\eta+\bar{\rho}\bar{\psi}\bar{u}_N N_\eta=0 \tag{17}$$

For these limiting equations at the far-field boundary, the appropriate boundary conditions are as follows:

a) At the wall $N=0$:

$$\bar{T}(0,1)=\bar{T}_w \text{ or } \bar{T}_N(0,1)=0$$

$$\bar{u}(0,1)=0,\quad \bar{\phi}(0,1)=0,\quad \bar{\psi}(0,1)=0$$

$$\bar{\theta}(0,1)=\bar{\psi}_N(0,1)N_\eta(0),\quad \bar{\Lambda}(0,1)=-1 \tag{18}$$

b) At the line of symmetry $N=S=1$:

$$\bar{T}(1,1)=1,\quad \bar{u}(1,1)=1,\quad \bar{\phi}_N(1,1)=0,$$

$$\bar{\psi}(1,1)=\bar{\phi}(1,1),\quad \bar{\theta}(1,1)=0,\quad \bar{\Lambda}(1,1)=0 \tag{19}$$

III. Numerical Method and Its Optimization

The numerical method employed uses a totally central-difference scheme, with an alternating-direction implicit (ADI) procedure for the solution of the governing differential equations. The method parallels that of Ghia,[12] with a significant amount of effort being directed in the present work toward improving and optimizing the numerical algorithm. Considerable success has now been achieved toward this goal. The actual study was carried out in the form of implementing three specific suggestions to accelerate the solution convergence rate. But before discussing these points, brief comments are made on the initialization, the convergence criterion used, and the nature of the solution domain.

Initialization, Convergence Criterion, Nature of Solution Domain

The initial conditions used are those given by Eqs. (28) in Ref. 12, with the additional variables $\bar{T},\bar{\rho}$, and $\bar{\mu}$ expressed in a manner similar to that for $\bar{u}$. The variable $\bar{\Lambda}$ is initialized as

$$\bar{\Lambda}(\eta,\zeta)=2\bar{u}(\eta,\zeta)-\frac{\bar{\phi}(\eta,\zeta)}{\bar{\psi}(\eta,\zeta)}\frac{\partial\bar{\rho}}{\partial\eta}(\eta,\zeta_{\max})$$
$$-\bar{u}(\eta,\zeta_{\max})-\bar{u}(\eta_{\max},\zeta) \tag{20}$$

This overall initialization procedure greatly helps in enhancing the convergence of the solution.

After examination of some standard convergence criteria, in view of the behavior of the corner-flow variables, it was decided to use the following definition for convergence:

$$\left[\sum_{i=1}^{N}\sum_{j=1}^{N}\text{Abs}(\bar{F}_{i,j}^{\eta+1}-\bar{F}_{i,j}^{*})\right]/N_p^2<\epsilon \tag{21}$$

where ϵ is a prescribed small number and N_p^2 is the total number of computational points. This criterion takes into consideration the number of grid points used and does not unnecessarily delay the overall convergence when only a small number of points do not satisfy the usual percentage-error criterion.

The present solutions have again verified that the ADI scheme used does not suffer from the nature of the flow domain. This is because the governing differential equations themselves, in addition to the symmetry conditions, are satisfied on the symmetry line which comprises a boundary of the triangular solution domain.

Relaxation of Outer Low-Shear Region

The three specific measures that led to significant improvements in the solution convergence rate are now discussed. The use of a nonuniform grid in the physical plane indeed helps to improve the accuracy of the numerical solution in the diffusion-dominated high-shear region near the walls. However, for stable numerical calculations, the time step required in this region is small. For the unbounded corner problem, use of the small inner-region time step everywhere leads to a slower convergence of the solution in the low-shear outer region of the unbounded domain of interest. To circumvent this difficulty, Ghia[12] had used time steps which varied spatially. This permits a larger time step in the low-shear region, thereby allowing the inner as well as the outer regions to relax to steady state in their natural relaxation times, without making the inner region relaxation time dominate the entire computation. For the solution of limiting equations at the far-field boundary, the following spatially dependent time step was employed[12]:

$$\Delta t_{\bar{F}}=\Delta t_{0,\bar{F}}[1+\bar{c}\eta] \tag{22}$$

where $\bar{c}$ is a constant. Numerical experiments conducted for the present study revealed that the simple function in Eq. (22),

with $\bar{c}=2$, is the most helpful in improving the solution convergence rate, leading to approximately 40% reduction in the required computer time. From this series of experiments, it was also found appropriate to introduce the spatially varying time steps only in the streamwise momentum equation and in the equation for $\bar{\psi}$.

One final comment to be made is that the same time step function must be used in both sweeps of the ADI method. This insures that, at a given point, the equations being solved during the two sweeps are consistent with the original differential equation. If this restriction is not honored, the solution diverges immediately.

Use of $\bar{\Lambda}$ in Governing Equations

The introduction of the dependent variable $\bar{\Lambda}$ in the governing differential equations leads to a considerable simplification of the equations for $\bar{\phi},\bar{\psi}$, and $\bar{\theta}$, and hence contributes to computational efficiency.[13] The computer time required was now approximately half of that required prior to the introduction of $\bar{\Lambda}$ and $\Delta t_{\bar{F}}(\eta)$.

Use of Coupling-Algorithm for Simultaneous Solution of $\bar{\theta}$-$\bar{\psi}$ Equations

From the mathematical formulation presented, it is clear that the solutions for the various dependent variables of the problem are mutually coupled through the governing equations (1-8). In addition, the modified streamwise-vorticity function $\bar{\theta}$ is also coupled to the velocity function $\bar{\psi}$ through the boundary condition at the wall. From the analysis of Ghia and Davis,[8] it is clear that an implicit treatment of the wall boundary condition leads to rapid convergence of the numerical solution. However, their implicit treatment of the boundary condition required the solution of two equations for $\bar{\theta}$ and two equations for $\bar{\psi}$ at each line of integration to obtain the homogeneous and particular solutions of the $\bar{\theta}$ and $\bar{\psi}$ equations, followed by proper superposition of these solutions. Instead, if the complete equations for $\bar{\theta}$ and $\bar{\psi}$ are solved simultaneously, this boundary condition on $\bar{\theta}$ can be treated implicitly without the need for making two sets of calculations to determine $\bar{\theta}$ and $\bar{\psi}$.

Although very attractive, this modification involves substantial changes in the associated computer program. However, the coupling algorithm is known[14] to improve considerably the efficiency of the numerical method. Therefore, it was decided to implement this algorithm in the present work also. The use of the coupling algorithm for the $\bar{\theta}$-$\bar{\psi}$ equations with appropriate time steps[15] led to about 25% increase in the convergence rate, so that the final computer time is about one-third of that prior to any optimization procedures.

To summarize the present effort toward optimization of the numerical solution, each of the three measures pursued helped significantly in reducing the overall computer time. For a test case ($M_\infty=1.5$ with adiabatic wall condition) with a (51×51) grid, which previously required 42 min on an I.B.M. 370/168 computer, use of $\bar{\Lambda}$ and the proper combination of time steps in the coupling algorithm leads to the result that the solution now requires 14 min to converge. For some of the other cases tested, the computational time has been reduced from the original 20 min to 7 min using these optimization procedures.

IV. Numerical Results and Discussion

Flow Parameters and Their Effect on Solution Convergence

The parameters appearing in the corner-flow formulation are the freestream Mach number M_∞, wall temperature $\bar{T}_w$, Prandtl number Pr, the viscosity law, and the freestream temperature T_∞ appearing through Sutherland's viscosity law. The first two parameters are of greater significance than the remaining ones, whose effects on the flowfield are discussed in Ref. 15.

It was observed that, for certain combinations of the flow parameters, the convergence rate of the numerical solution was very slow. Moreover, the test cases did not exhibit any trend about the convergence rate of the solutions for variation in M_∞ and $\bar{T}_w$. However, when the thermal ratio R, defined as $R=\bar{T}_w/\bar{T}_0$, with $\bar{T}_0$ being the stagnation temperature, was considered as a parameter rather than $\bar{T}_w$, a traceable trend emerged for the behavior of the solution convergence rate with the variation in this flow parameter. In general, the adiabatic cases ($R=1$, if the model fluid assumption is used) requires more iterations for convergence, while the solution convergence rate improves significantly as R decreases. Using the physical characteristics of the flow as a guideline, the suitable time step $\Delta t_{\bar{F}}$ for each equation, for values of the parameters M_∞ and $\bar{T}_w$ intermediate to the values tested, was deduced from the values of the time steps determined for the test cases. Satisfactory convergence rates for the solution for these intermediate cases assured the importance and usefulness of such a study.

Comparison of Results with Solutions for Some Limiting Cases

The mathematical model formulated is validated, at least partially, by obtaining numerical solutions for two degenerate cases. First, the results of Ghia[12] for the incompressible flow along an infinite axial corner are reproduced. Second, the viscous asymptotic solutions at the far-field boundary $\zeta\to\infty$, for a real fluid, are compared with the corresponding results of Ghia and Davis.[9] Satisfactory agreement with both of these available results gave some reliance on the present formulation.

Next, solutions are obtained for the finite-corner flow configurations studied by Weinberg and Rubin[7] for compressible flow with the model-fluid assumption. In their study for adiabatic and cold wall ($R=0.6$) cases, M_∞ was varied between zero and 2, including $M_\infty=0.95$. The results obtained agree satisfactorily with those of Ref. 7; next, the assumptions used in the latter analysis are assessed. In the results to be presented now, the case with $M_\infty=0.95$ is included only for the purpose of comparison. As the corresponding inviscid flow for this case has not been analyzed using transonic flow theory, the results must be viewed with caution due to the approximation involved in the matching condition.

Effect of Location of Far-Field Boundary and Use of Model-Fluid Assumption

Two sets of results are obtained using the present analysis. In one set, the model-fluid assumption is used, with the far-field boundary placed at true infinity; the second set of results is generated without the assumption of model fluid, i.e., for a real fluid. These results, together with those of Weinberg and Rubin[7] for a finite corner with $\zeta_{\max}=9.6$, are depicted in Figs. 2 through 7. The results are classified into two groups —adiabatic cases, and heat-transfer cases—which are discussed next.

Adiabatic Cases

The streamwise skin-friction coefficient is depicted in Fig. 2 with M_∞ as a parameter. The model-fluid assumption does not influence the skin-friction coefficient very noticeably, but the location of the far-field boundary at a finite value of $\zeta_{\max}$ underpredicts the skin-friction coefficient. The inset in this figure shows the skin friction decreases with increase in M_∞, i.e., with increase in the extent of the viscous region. The results for the streamwise and crossflow velocities as well as the temperature field are qualitatively similar[15] to those for the heat-transfer cases which are discussed next.

Heat-Transfer Cases

The streamwise velocity $\bar{u}$ along the symmetry line is plotted in Fig. 3 for various values of M_∞. The effect of

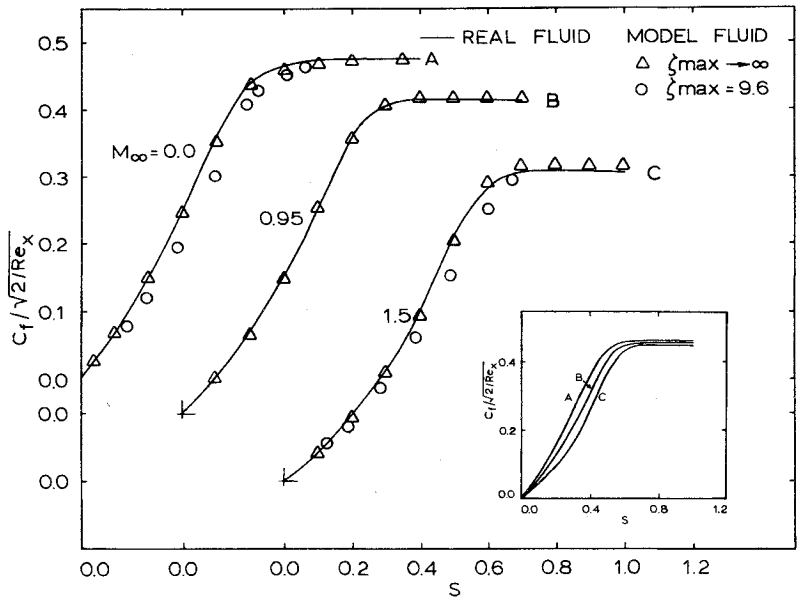

Fig. 2 Streamwise skin-friction distribution—adiabatic wall.

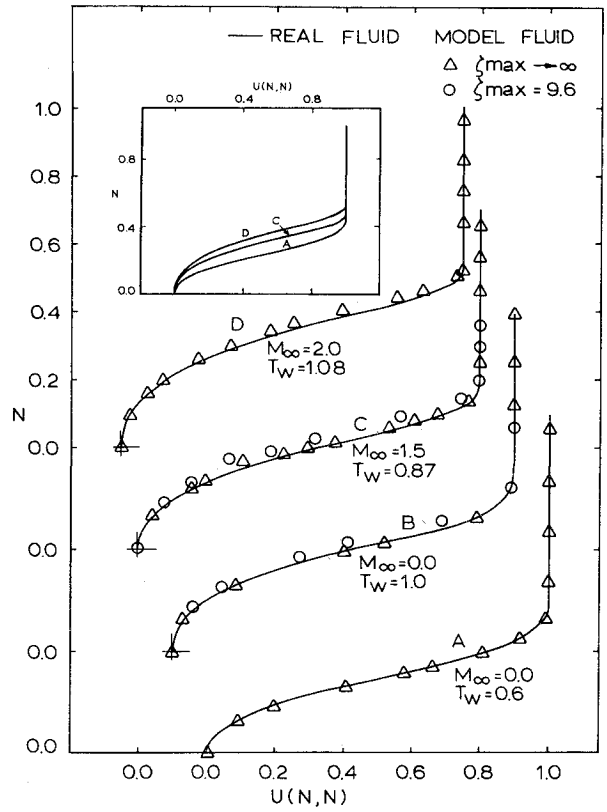

Fig. 3 Streamwise velocity along symmetry line—various wall temperatures.

location of the far-field boundary is more pronounced. Use of a finite value of ζ_{max} leads to a tendency to underpredict the $\bar{u}$ velocity; this effect increases with increase in Mach number. This figure also shows that the deviation due to the model-fluid assumption is significant only at higher Mach numbers. The corresponding crossflow velocity $\bar{w}$ is presented in Fig. 4, which shows that the effect of placing the far-field boundary at a finite distance is to overpredict the crossflow velocity. The assumption of a model fluid also leads to a tendency to overpredict the $\bar{w}$ velocity and to increase the degree of swirling flow, which increases further with the increase in M_∞. On the other hand, from curves A and B, it can be seen that cooling the flow has a tendency to relieve some of this swirl. Figure 5 shows the variation of the static temperature along the symmetry line for various Mach numbers. The effect of location of the far-field boundary is not significant. However, the effect of the model-fluid assumption is to slightly overpredict the temperature; this effect is more pronounced around the location $N=0.4$. Also, there is an overshoot in the temperature profiles (curves C and D); this overshoot increases significantly with increase in M_∞, creating zones of high temperature.

The streamwise skin-friction coefficient is depicted in Fig. 6. The effect of the location of the far-field boundary is to underpredict the skin-friction values; this effect increases with increasing Mach number. On the other hand, the effect of model-fluid assumption is not significant, except for the cold wall case (curve A). Further, as M_∞ increases the extent of the viscous region also increases, thereby decreasing the skin-friction parameter as shown in the inset in this figure. Figure 7 gives the heat-transfer coefficient for various wall temperatures and Mach numbers. The effect of the location of the far-field boundary is slightly to underpredict the heat-transfer coefficient, whereas the results for model fluid show significant deviation from those of real fluid. Also, this deviation increases considerably as $\bar{T}_w$ decreases from a value 1.08 for curve D to 0.6 for curve A. As seen in Fig. 7, the deviations in the heat-transfer coefficient are maximum as the asymptotic state is approached. These deviations are primarily due to differences in Pr. The present asymptotic results, conform to the available empirical expression, $C_h = C_f/2\ Pr^{2/3}$, for flow past a flat plate. For aerodynamic heating design considerations, the heat-transfer coefficient is a significant quantity and the deviations seen in Fig. 7 support the need for the present analysis without the assumption of model fluid.

Effect of M_∞ and $\bar{T}_w$ on the Results for Real-Fluid Cases

Numerical solutions for real-fluid cases are obtained for freestream Mach number M_∞ ranging from 0 to 4 and for the wall boundary condition on temperature corresponding to an adiabatic wall or to values of the thermal ratio R varying from 0.1 to 1.5. The latter condition corresponds to cases with nonzero heat transfer across the wall.

The streamwise skin-friction coefficient C_{fu} along the plate surface $N=0$, is presented in Fig. 8. For a fixed wall temperature condition, as M_∞ increases, it increases the extent of the viscous region and, consequently, decreases the

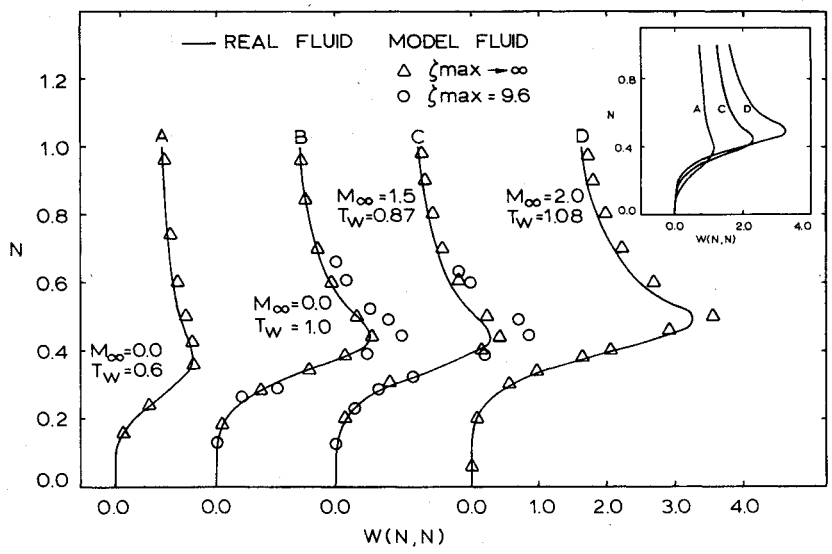

Fig. 4 Crossflow velocity along symmetry line—various wall temperatures.

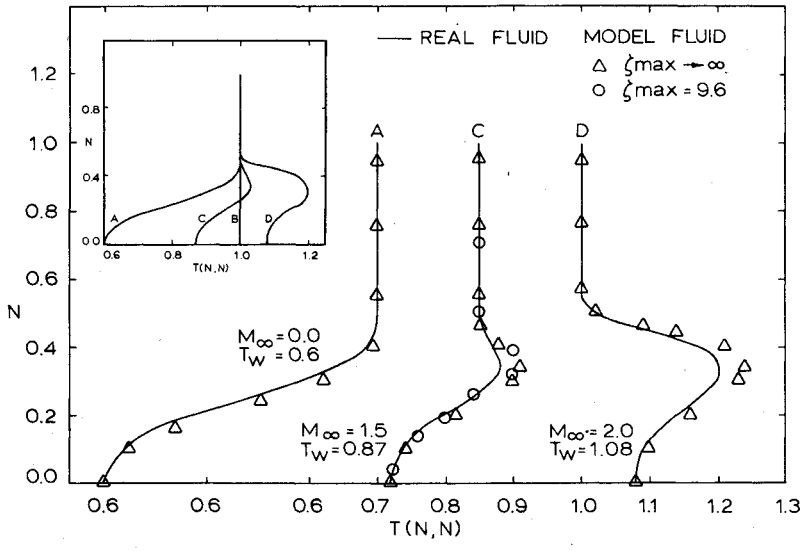

Fig. 5 Temperature along symmetry line—various wall temperatures.

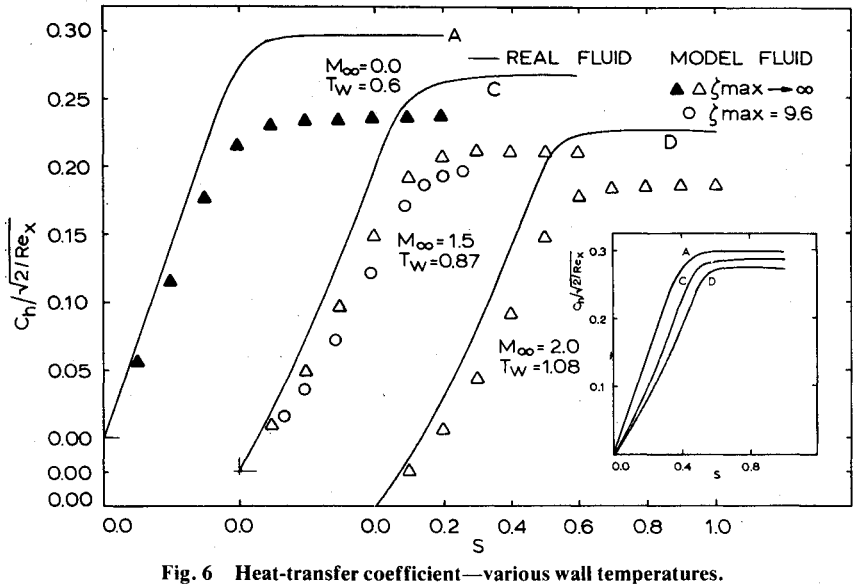

Fig. 6 Heat-transfer coefficient—various wall temperatures.

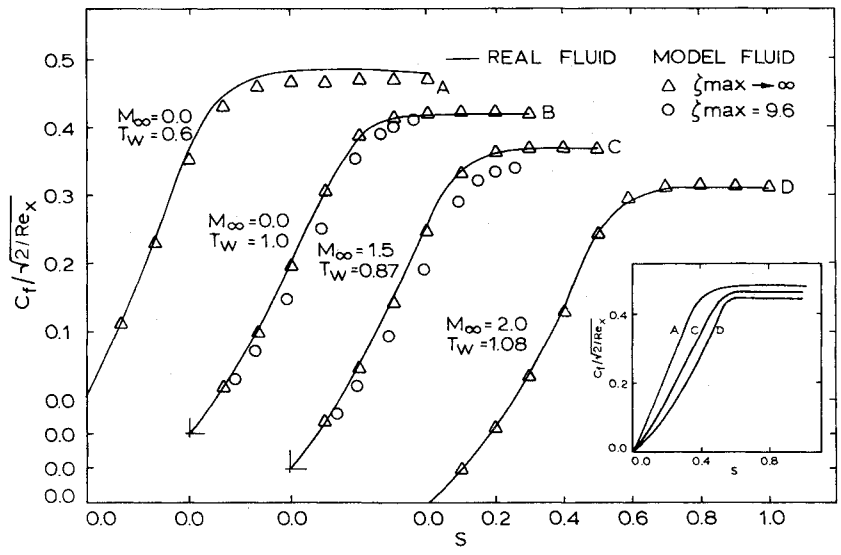

Fig. 7 Streamwise skin-friction distribution—various wall temperatures.

streamwise skin-friction coefficient. A similar effect is also observed for the cases with $M_\infty = 2.0$, when the wall temperature condition is varied from the cold wall case of $R = 0.3$, through $R = 0.6$, to the adiabatic wall case. On the other hand, for $M_\infty = 4.0$, the adiabatic wall case shows a higher value of skin friction as compared to the cold wall cases, in the high-shear region of the corner. Also, a somewhat irregular behavior is observed in this figure for the C_{f_u} curve between $S \simeq 0.5$ and 0.7 for the adiabatic wall, with $M_\infty = 4.0$; this will be soon discussed here. Finally, the heat-transfer coefficient C_h along the plate surface $N = 0$ is depicted in Fig. 9. For a fixed wall temperature condition, as M_∞ increases, the heat-transfer coefficient decreases, with a similar effect being observed for fixed M_∞, with increase in the values of R.

Some additional results for $M_\infty = 2$ and 4 have been presented in Ref. 15. From those results and Figs. 8 and 9, it is seen that the results for $M_\infty = 4$ do not conform to the general trends observed for those up to $M_\infty = 3$. Therefore, the case of $M_\infty = 4$ is examined further.

Examination of Results for $M_\infty = 4.0$ and Comments on Limitations for the Range of Parameters

The results for the case of $M_\infty = 4.0$ with various wall temperature conditions were further examined closely in an attempt to understand the cause for some irregular behavior observed in Fig. 8 for the C_{f_u} curve near $S \simeq 0.5$. The irregularity is found to disappear completely when the thermal ratio R is decreased to 0.1. This has led to the inference that the irregular behavior observed earlier may not be solely due to the mesh spacing used in the discretized problem. In fact, a step size study for the adiabatic case with $M_\infty = 4.0$ has confirmed that the (51×51) grid employed is adequate for all of the dependent variables except for the crossflow velocity $\bar{w}$ and the skin-friction coefficient C_{f_u}, both of which show a maximum of 6% variation with grid refinement. For a coarser grid, the irregular behavior in skin-friction coefficient is more pronounced and, as seen in Fig. 8 for the present case of (51×51) grid, it appears around $S \simeq 0.5$ where the crossflow velocity has a steep rise in its value. It is conceivable that, for such a combination of the flow parameters, a further clustering of the grid points in the vicinity of $N = S = 0.5$ could lead to better representation of the flow in this region and alleviate this behavioral problem. This explanation is further supported by the case corresponding to $R = 0.1$, where the swirl intensity decreases significantly and, as such, shows no irregularity in the C_{f_u} distribution. Thus, the cases with $M_\infty = 4.0$ represent an upper limit for the uniform (51×51) grid in the (N,S) plane.

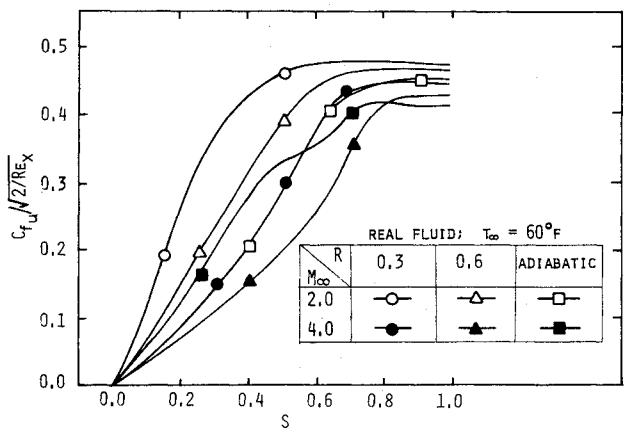

Fig. 8 Effect of M_∞ and $\bar{T}_w$ on streamwise skin-friction coefficient.

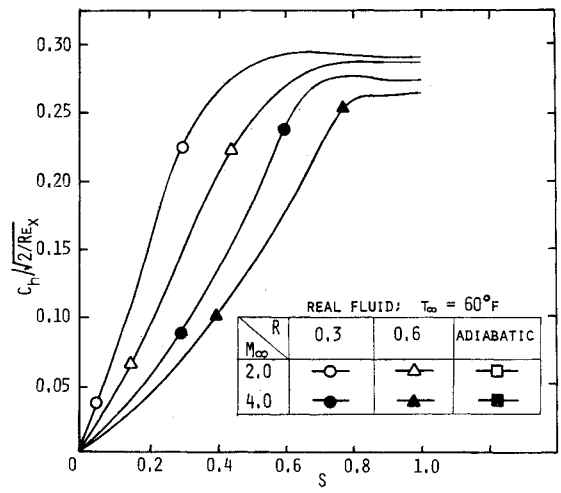

Fig. 9 Effect of M_∞ and $\bar{T}_w$ on heat-transfer coefficient.

To place the present analysis in proper perspective, it is appropriate to comment, at this juncture, on the range considered by Weinberg and Rubin[7] for M_∞ and wall temperature. They had experienced considerable difficulty in the convergence of the numerical algorithm as the thermal ratio R was decreased, and were unable to obtain converged solutions for $R < 0.6$ with $\zeta_{max} = 9.6$. In their finite-corner analysis, the streamwise vorticity function θ grows very rapidly as T_w

decreases and the gradients of θ become large enough to perhaps preclude convergence of the solution. Also, an asymptotic analysis shows that the skin-friction coefficient behaves as $C_{f_u} \sim (1+\chi/\zeta^2)$, where χ is a parameter which depends on compressibility effects. If χ becomes positive, C_{f_u} will exhibit an overshoot at intermediate values of ζ, before approaching its final asymptotic value for $\zeta \to \infty$. Indeed, χ becomes positive for $M_\infty > 2.0$ and $R \leq 0.4$, and this led Weinberg and Rubin[7] to work with the limits $0 \leq M_\infty \leq 2$ and $R \geq 0.6$. Nevertheless, their results have been very helpful in the course of the present study. Although Weinberg and Rubin[7] have underestimated their limits on the range of M_∞ and R from a computational viewpoint, they are right in their concern about the importance of hypersonic interaction effects for higher M_∞. The onset of these effects may dominate the flow and render the present numerical solutions with the assumption of shock-free supersonic flow physically invalid. However, to obtain accurate and rapidly converging numerical solutions for parameters near these limiting values, some additional refinements are suggested; these are now described.

Refinements for Highly Supersonic Flows

For corner-flow configurations with freestream Mach number $M_\infty > 2.0$, two major difficulties were encountered. The grid distribution used may not provide adequate resolution in the regions of high gradients and, as such, the accuracy of the solutions becomes unsatisfactory. Also, the solution convergence rate is not satisfactory as M_∞ increases. To overcome these difficulties, the use of a "numerical density-transformation" and a "hybrid-difference scheme" is suggested.

In order to improve the distribution of grid points for highly supersonic flow in the corner, ideally it would be desirable to employ a three-dimensional density transformation; but this, to the best knowledge of the authors, does not presently exist. At first, appropriate two-dimensional compressibility transformations were considered in the present work, with the understanding that, although they may not totally eliminate the appearance of density from the governing differential equations, they may help to provide the necessary resolution and may, thereby, lead to more accurate and efficient solutions for high Mach number flows. This suggestion was not actually implemented as, in the course of this study, it became clear that the mapping functions $N=N(\eta)$ and $S=S(\zeta)$ used can themselves be suitably modified to incorporate a "density transformation" in them.[13] The new density-strained coordinates are thus defined as

$$\bar{\eta} \triangleq \int_0^\eta \rho(\eta, \infty)\, d\eta \tag{23a}$$

$$\bar{\zeta} \triangleq \int_0^\zeta \rho(\infty, \zeta)\, d\zeta \tag{23b}$$

These transformations need prior knowledge of $\rho(\eta,\infty)$ and $\rho(\infty,\zeta)$, which can be obtained easily by first solving the limiting equations at the far-field boundary as $\zeta \to \infty$ using the original $N=N(\eta)$ transformation. The density-strained coordinate $\bar{\eta}$ is then determined numerically using Eq. (23a), with $\bar{\zeta}$ being directly obtained from $\bar{\eta}$, using the symmetry of the problem. Thereafter, the overall mapping functions $N=N(\bar{\eta})$ and $S=S(\bar{\zeta})$ are also determined numerically. Although explicit analytical relations do not exist, for example, between N and $\bar{\eta}$, the derivatives of the mapping functions needed in the flow equations are easily determined in this manner (see Ref. 13).

As stated earlier, the solution convergence rate becomes considerably slow as the Mach number of the flow increases. For a stable sequence of calculations for these high M_∞ cases, the permissible time steps become very small in order to simultaneously assure diagonal dominance of the resulting coefficient matrix and, consequently, satisfy the cell Reynolds number limitations. It was obvious that the use of an upwind-differencing scheme (UDS) in the low-shear region, where convective terms dominate, could help to improve the stability of the scheme and, hence, the convergence of the algorithm. However, in order to avoid any oscillations in the solution by switching abruptly from a central-difference scheme (CDS) to UDS at a prescribed value of η, namely η_p, the switch was made in a gradual manner. This may be achieved, for example, by using the following relation when UDS locally acquires a forward-difference representation:

$$\left.\frac{\partial F}{\partial \eta}\right|_{i,j} = \frac{1}{2\Delta\eta}\left[2w_0\left(F_{i+1,j}-F_{i,j}\right) + \left(1-w_0\right)\left(F_{i+1,j}-F_{i-1,j}\right)\right] \tag{24}$$

where the weighting factor w_0 is defined as

$$w_0 = \begin{cases} 0 & \eta \leq \eta_p \\ 1 - \dfrac{\eta_p}{\eta} & \eta > \eta_p \end{cases}$$

This scheme is referred to as the "hybrid-differencing" scheme. The results obtained with this scheme are considered to be accurate as they compare well with those obtained using total CDS and are not very sensitive to the choice of η_p or to the choice of time steps. The second-order-accurate diagonally dominant scheme of Khosla and Rubin[16] was also implemented and was found to be equally satisfactory.

The mapping functions which include the "density transformation" were implemented in the present work together with the "hybrid-differencing" scheme. Numerical results obtained for a test case show an additional saving of about 15% in the computational time. These new results do show a maximum deviation of about 7% in the $\bar{w}$ velocity and 5% in the C_{f_u} distribution, as compared to results obtained without the "density transformation" or the "hybrid-differencing" scheme. However, without any available experimental data, the question of accuracy cannot be completely answered. From these observations, it can be stated that partial success has been achieved in alleviating the computational difficulties associated with simulating three-dimensional highly supersonic flows.

V. Conclusion and Recommendations

Compressible shock-free flow of a real fluid along an unbounded 90-deg axial corner has been analyzed considering viscous interactions. Numerical solutions have been obtained for a wide range of freestream Mach number and various thermal conditions at the wall, with arbitrary Prandtl number and Sutherland's viscosity law. The present results constitute the first available solutions for the general compressible viscous corner flows. Although the general trends remain similar, the combined effect of the assumption of model fluid and the use of a finite-corner region, is not negligible. The assumption of a model fluid has a tendency to increase the swirling motion and the level of static temperature inside the corner; it also considerably underpredicts the heat-transfer coefficient. Effects of other flow parameters such as Prandtl number and viscosity law are not very significant except on the C_n. Effect of mass transfer at the corner walls has also been studied and will be reported in the near future.

The procedures developed for the numerical analysis and solution of the corner problem are proving useful in the numerical solution of other flow problems also. It is clear that the coordinate system used in the analysis is not completely suitable. An orthogonal coordinate system having a single coordinate surface aligned to both corner walls[17] is highly

desirable. However, these coordinates should be such that the far-field boundary condition can be properly formulated. It is also important that the new coordinate system be obtained for a corner geometry with a variable included angle,[18] so that more general corner configurations may be analyzed with the formulation. Recently, Shang and Hankey[19] have been successful in analyzing the compressible corner problem with one compression surface using the complete three-dimensional Navier-Stokes equations. Their solutions provide the detailed complex flow structure including shocks, and very satisfactorily verify the experimental data of Cooper and Hankey.[20] For more involved configurations, an analysis of the type performed in the present study would provide carefully computed asymptotic solutions to the full Navier-Stokes equations for the corner layer.

Acknowledgment

The authors wish to express their sincere appreciation to U. Ghia for her many valuable discussions and to R. T. Davis for his useful suggestions in the course of this study. This research was supported by the Aerospace Research Laboratory under Contract No. F 33615-73-C-4014. This paper is based on the Ph.D. disseration of the first author.

References

[1] Korkegi, R. H., "Survey of Viscous Interactions with High Mach Number Flight," *AIAA Journal*, Vol. 9, May 1971, pp. 771-784.

[2] Charwat, A. F. and Redekeopp, L. G., "Supersonic Interference Flow Along the Corner of Intersecting Wedges," *AIAA Journal*, Vol. 5, Mar. 1967, pp. 480-488.

[3] Kutler, P., "Supersonic Flow in the Corner Formed by Two Intersecting Wedges," *AIAA Journal*, Vol. 12, May 1974, pp. 577-578.

[4] Bloom, M. H., Rubin, S. G., and Cresci, R., J., "Three-Dimensional Viscous Interactions," *Proceedings of the Symposium on Viscous Interaction Phenomena in Supersonic and Hypersonic Flows*, Dayton University Press, 1969, pp. 493-511.

[5] Rubin, S. G., "Incompressible Flow Along a Corner," *Journal of Fluid Mechanics*, Vol. 26, Sept. 1966, pp. 97-110.

[6] Rubin, S. G. and Grossman, B., "Viscous Flow Along a Corner: Numerical Solution of the Corner Layer Equations," *Quarterly of Applied Mathematics*, Vol. 29, July 1971, pp. 169-186.

[7] Weinberg, B. C. and Rubin, S. G., "Compressible Corner Flow," *Journal of Fluid Mechanics*, Vol. 56, Dec. 1972, pp. 753-774.

[8] Ghia, K. N. and Davis, R. T., "Corner Layer Flow: Optimization of Numerical Method of Solution," *Computers and Fluids*, Vol. 2, March 1974, pp. 17-34.

[9] Ghia, K. N. and Davis, R. T., "A Study of Compressible Potential and Asymptotic Viscous Flows for Corner Region," *AIAA Journal*, Vol. 12, March 1974, pp. 355-359.

[10] Libby, P. A., "Secondary Flows Associated with a Supersonic Corner Region," *AIAA Journal*, Vol. 4, June 1966, pp. 1130-1132.

[11] Bloom, M. H., "Remarks on Compressibility Effects in the Boundary Layer Cross Flow Near a Corner," Polytechnic Institute of Brooklyn, Brooklyn, N.Y., PIBAL Rept. 969, 1966.

[12] Ghia, K. N., "Streamwise Flow Along an Unbounded Corner," *AIAA Journal*, Vol. 13, July 1975, pp. 902-907.

[13] Mikhail, A. G., "Analysis and Numerical Solution of General Compressible Viscous Flow Along a 90° Axial Corner," Ph.D. Thesis, Univ. of Cincinnati, Aug. 1976.

[14] Ghia, U. and Ghia, K. N., "Numerical Generation of a System of Curvilinear Coordinates for Turbine Cascade Flow Analysis," Univ. of Cincinnati, Rept. No. AFL 75-4-17, 1975.

[15] Mikhail, A. G. and Ghia, K. N., "Study of Viscous Compressible Flow Along an Axial Corner," AIAA Paper 77-685, Albuquerque, N. Mex., June 1977.

[16] Khosla, P. K. and Rubin, S. G., "A Diagonally Dominant Second-Order Accurate Implicit Scheme," *Computers and Fluids*, Vol. 2, Aug. 1974, pp. 207-209.

[17] Tokuda, N., "Viscous Flow Near a Corner in Three Dimensions," *Journal of Fluid Mechanics*, Vol. 53, May 1972, pp. 129-348.

[18] Desai, S. S. and Mangler, K. W., "Incompressible Laminar Boundary-Layer Flow Along a Corner Formed by Two Intersecting Planes," Royal Aircraft Establishment, Farnborough, England, RAE TR 74062, Aug. 1974.

[19] Shang, J. S. and Hankey, W. L., "Numerical Solution of the Compressible Navier-Stokes Equations for a Three-Dimensional Corner," AIAA Paper 77-169, Jan. 1977; also *AIAA Journal*, Vol. 15, Nov. 1977, pp. 1575-1582.

[20] Cooper, J. R. and Hankey, W. L., "Flowfield Measurements in an Axisymmetric Axial Corner at $M = 12.5$," *AIAA Journal*, Vol. 12, Oct. 1974, pp. 1353-1357.